This is a preprint, the final version is subject to change, of the American Mineralogist (MSA)
Cite as Authors (Year) Title. American Mineralogist, in press.
DOI: https://doi.org/10.2138/am-2018-6582

**Revision 2**

# Dating phosphates of the strongly shocked Suizhou chondrite

Shaolin Li[1,2] and Weibiao Hsu[3*]

[1]Purple Mountain Observatory
Chinese Academy of Sciences
Nanjing 210034
China

[2]School of Astronomy and Space Sciences
Nanjing University
Nanjing 210093
China

[3]Space Science Institute,
Macau University of Science and Technology
Macau

*Corresponding author's e-mail: wbxu@pmo.ac.cn

This is a preprint, the final version is subject to change, of the American Mineralogist (MSA)
Cite as Authors (Year) Title. American Mineralogist, in press.
DOI: https://doi.org/10.2138/am-2018-6582

# Dating phosphates of the strongly shocked Suizhou chondrite

## ABSTRACT

Impacts on undifferentiated asteroidal bodies provide invaluable information for understanding the Solar System evolution. Nevertheless, dating early and small-scale impact events is technically challenging. Uranium–lead (U–Pb) systematics of U-bearing phases within shock-induced melt veins (SMVs) of chondrites may be significantly disturbed by localized heating, thus providing opportunities to date these impact events. As one of the major U hosts in chondrites, apatite in the Suizhou (L6) chondrite has been compositionally and structurally modified to varying degrees by shock metamorphism. Apatite grains in the host remained largely intact during the impact and have recorded the initial thermal cooling time (~4550 Ma) on their parent body. Apatite grains in regions less than 100 μm bordering the SMVs or in relatively "cold" regions within the SMVs were partly decomposed to tuite, driven by the localized transient heating within the SMVs. Their U–Pb systematics have been disrupted to varying extents. Apatite in regions close to the center of the SMVs has been completely transformed to tuite, which yields an age of 4481 ± 30 Ma (2σ), providing an upper limit to the impact event. This study clearly demonstrates that by integrating *in situ* U–Pb isotope analysis with detailed microstructural and compositional analysis of phosphates, it is possible to deduce the timing of early and small-scale celestial impact events, hence a more comprehensive understanding of the impact history of the Solar System.

**Key words** Apatite, tuite, L chondrite, *in situ* U–Pb dating, early impacts in the Solar System

This is a preprint, the final version is subject to change, of the American Mineralogist (MSA)
Cite as Authors (Year) Title. American Mineralogist, in press.
DOI: https://doi.org/10.2138/am-2018-6582

# INTRODUCTION

Impacts occur during all stages of planet formation and evolution, from the initial accretion of chondritic materials in the nebula, to differentiation and secondary alteration on planetary bodies (Scott, 2002). Due to impact-induced heating, isotopic chronometers of target rocks can be reset and record the timing of these impact events (Deutsch and Schärer, 1994; Bogard, 1995; Jourdan et al., 2009). However, impact ages are not always straightforward to be interpreted, largely due to the lack of knowledge about how shock metamorphism affects isotopic systematics in specific minerals and in whole rocks (e.g., Deutsch and Schärer, 1994; Niihara et al., 2012; El Goresy et al., 2013; Bloch and Ganguly, 2014; Darling et al., 2016).

One fundamental question is whether the isotopic chronometer is disturbed during shock compression or the prolonged post-shock annealing (Deutsch and Schärer, 1994; El Goresy et al., 2013). Laboratory shock recovery experiments have been performed, followed by isotopic analysis, to decipher the relationship between the degree of shock metamorphism and isotopic disturbance since 1960s (e.g., Fredriksson and De Carli, 1964; Bogard et al., 1987; Deutsch and Schärer, 1990; Gaffney et al., 2011; Niihara et al., 2012). Shock compression, up to ~60 GPa, can hardly disturb a series of isotopic chronometers (e.g., Sm–Nd, Rb–Sr, U–Pb and K–Ar), although slight $^{40}$Ar loss was observed for higher shock pressures (Bogard, 1995). The general conclusion drawn from these experiments is that post-shock annealing plays the most important role in resetting isotopic chronometers, and naturally shocked and unannealed samples are unlikely to record the timing of the impact event (Deutsch and Schärer, 1994). However, the duration of the high-pressure regime in laboratory

recovery experiments is several orders of magnitude shorter than shock pulse in natural impact events (Sharp and DeCarli, 2006). This casts doubt on whether the results obtained from recovery experiments are readily applicable to natural impact events on planetary bodies (El Goresy et al., 2013).

Natural impacts can induce localized melting by shear stress along the grain boundaries of minerals with different shock impedance, frictional heating along shear zones, and collapse of pores during shock compression (Sharp and DeCarli, 2006). Shock melt veins (SMVs) generated in these processes could reach temperatures and pressures in excess of 2500 °C and 26 GPa (Langenhorst and Poirier, 2000; Sharp and DeCarli, 2006; Gillet and El Goresy, 2013). Various high-pressure phases can form in these SMVs under the extreme *P–T–t* conditions, either through solid-state transformation or crystallization from the dense silicate melt. Tuite, with the structure of trigonal γ-$Ca_3(PO_4)_2$, was first identified in the SMVs of the Suizhou L6 chondrite (Xie et al., 2002) as a high-pressure polymorph of merrillite and later in other meteorites, such as Martian and iron meteorites (e.g., Fritz and Greshake, 2009; Litasov and Podgornykh, 2017). It was also suggested that tuite could be formed by decomposition of apatite through the reaction: $2Ca_5(PO_4)_3X \rightarrow 3\gamma\text{-}Ca_3(PO_4)_2 + CaX_2$ (Murayama et al., 1986; Xie et al., 2013), where X represents monovalent anions that are dominated by $Cl^-$ in equilibrated L chondrites (Lewis and Jones, 2016). Because phosphates are the major U hosts in chondrites (Göpel et al., 1994), tuite formed during impact events has great potential to date these processes. In this contribution, we present *in situ* U–Pb dating of tuite and apatite in the strongly shocked Suizhou chondrite. This is the first report of U–Pb dating on a high-pressure phase of phosphates. The U–Pb systematics of tuite provides insights into whether and to what extent it could

be affected by the extreme *P–T–t* regime during natural impacts.

# SAMPLE AND ANALYTICAL METHODS

## Sample

The sample used in this study is a witnessed fall, the Suizhou chondrite (L6), which fell in Suizhou, China in 1986. It was strongly shocked (S4-S5; Xie et al., 2001), with olivine and pyroxene exhibiting weak mosaic textures and plagioclase being partly (~30 vol%) transformed to maskelynite. The meteorite contains a few thin black SMVs (mostly 0.02–0.09 mm in width). Up to 12 high-pressure phases were identified in the SMVs, including ringwoodite, bridgmanite (vitrified), majorite, majorite-pyrope garnet, akimotoite, hemleyite, magnesiowüstite, lingunite, wangdaodeite, xieite and a $CaFe_2O_4$-polymorph of chromite and tuite (Xie and Chen, 2016 and references therein). The assemblage of majoritic garnet + ringwoodite + magnesiowüstite in the SMVs suggests crystallization temperature about 1800–2000 °C under pressure of 20–22 GPa (Xie et al., 2001). The presence of akimotoite, devitrified perovskite and xieite inside and directly adjacent to the SMVs suggests that the maximum pressure and temperature developed in the Suizhou SMVs could reach about 24 GPa and 2200 °C (Xie and Chen, 2016). Under the estimated *P–T* condition, tuite in Suizhou could have been transformed from both merrillite and apatite (Xie et al., 2013).

## Analytical methods

Five polished sections are carbon-coated before petrographic investigation using scanning electron microscope (SEM). Phosphates in the vicinity of the SMVs of Suizhou were identified using X-ray mapping with the Oxford X-Max energy-dispersive spectrometer equipped on the Hitachi

S-3400N SEM at Purple Mountain Observatory (PMO), Chinese Academy of Sciences. Cathodoluminescence (CL) images of the phosphates were obtained using a MonoCL4 system attached to the SEM with a 15 kV accelerating voltage.

Raman spectra of phosphates were collected at PMO, using a Thermo Scientific DXR confocal laser Raman spectrometer. The 532 nm wavelength solid laser was focused on a spot less than 1 μm to excite the Raman signal. The laser power was limited to 1–3 mW to avoid deterioration of minerals due to laser heating. Accumulations of 200–300 seconds were made for each measurement. A step size of 1 μm and an accumulation time of 4 s were utilized for point-by-point Raman mapping. During the Raman mapping, fluorescence interferences in the background were very low and basically negligible.

Major- and minor- element compositions of phosphates were determined with a JEOL 8230 electron microprobe analysis (EPMA) at PMO. An acceleration voltage of 15 kV and a probe current of 20 nA were used during each analysis. Both standards and samples were analyzed with a beam diameter of 5 μm to minimize volatilization of halogens in apatite. Counting duration was 20 s for all elements. The following standards were used for calibration: fluorapatite for Ca, P, and F; olivine for Mg and Fe; tugtupite for Cl; albite for Na; rhodonite for Mn; synthetic cerium fluoride ($CeF_3$) for Ce. The detection limit(s) for F and Cl were 0.04 and 0.01 wt%, respectively; for $Ce_2O_3$ was 0.06 wt% and for all other oxides were 0.01–0.03 wt%.

*In situ* U–Pb isotopic analysis of phosphates in Suizhou was performed on a large-geometry, double-focusing CAMECA ims-1280 HR secondary ion mass spectrometer (SIMS) at the institute of Geology and Geophysics, Chinese Academy of Sciences in Beijing. The detailed analytical procedure for U–Pb dating of phosphates was described in Li et al. (2012). It has been successfully applied to

meteoritic phosphates (e.g., Popova et al., 2013; Zhou et al., 2013; Yin et al., 2014; Li and Hsu, 2018a; 2018b; 2018). To minimize potential Pb contamination during sample preparation, all sections were cleaned with ethanol and de-ionized water in an ultrasonic bath after removing previously-coated carbon films, and were re-coated with carbon before SIMS analysis. Because phosphates in the SMVs are mostly small in size (mostly < 20 μm), $O^-$ was chosen over $O_2^-$ as the primary ion beam as it has higher density hence a smaller beam diameter (Liu et al., 2011). For the same reason, the Gaussian illumination mode of the primary beam was used with a 200 μm diameter aperture. A focused primary beam (10 × 15 $\mu m^2$) was finally obtained. The $O^-$ primary ion beam was accelerated at –14 kV with an intensity of 5–7 nA. The stimulated secondary ions were accelerated at a potential of +10 kV. The dynamic multi-collector analysis technique was used to acquire high-precision $^{207}Pb/^{206}Pb$ ratios as in the static multi-collector mode without trade off in the analytical precision of the $^{238}U/^{206}Pb$ ratio of the conventional peak-hopping mono-collector mode (Liu et al., 2015). $^{40}Ca_2{}^{31}P^{16}O^{3+}$ was used as a reference peak at mass resolution of 8000 (defined at 50% height) for tuning of secondary ions, energy and mass adjustments. Each spot was pre-sputtered on a square area (35 × 35 μm) for 120 s to remove the surface contamination and to enhance the secondary ion yields. Each measurement consists of 15 cycles, with the total analytical time of about 26 min.

Calculation of the U–Pb ages of the samples requires consideration for matrix effects resulting from differences in mineral chemistry and crystal structure between samples and standards. Although the matrix effects would be less significant in our apatite analyses, the lack of a suitable tuite standard means that the tuite analyses were necessarily corrected with the apatite standard NW–1 (1160 Ma; Li et al., 2012). Due to insufficient number of SIMS analyses on tuite, the uncertainty induced by matrix

effects in tuite U–Pb age is difficult to be quantified. The uranium concentrations were calibrated relative to the Durango apatite, which contains approximately 9 ppm of U (Trotter and Eggins, 2006). The U–Pb and Pb–Pb ages were calculated with the revised $^{238}U/^{235}U$ ratio (137.79; Goldmann et al., 2015) using Isoplot/Ex ver. 3.75 (Ludwig, 2012). Compared with the canonical $^{238}U/^{235}U$ value of 137.88, the Pb–Pb ages of phosphates in Suizhou were reduced by ~0.95 My. The uncertainty for the U-Pb and Pb-Pb ages are given at the 95% confidence level unless otherwise specified.

# RESULTS

## Texture and chemistry of phosphates

Apatite in the host of Suizhou (H-ap) contains three sets of planar fractures. But in most cases, only one or two sets are visible (Figs. 1a–c). H-ap is homogenous and has an average Cl content of 5.61 wt%, with minor $Na_2O$ (~0.42 wt%), and is nearly free of MgO (< 0.01 wt%) (Fig. 2; Table 1; please see the supplementary material for complete results of EPMA analysis). The Raman spectrum of H-ap is characterized by an intense peak at 960 $cm^{-1}$, three less intense peaks at 427, 589, and 1038 $cm^{-1}$, and two weak peaks at 612 and 1077 $cm^{-1}$ (Fig. 3), which are typical for unshocked chlorapatite (Xie et al., 2013).

Apatite grains adjacent to the wall of the SMVs (W-ap) exhibit two distinctive (dark and bright) parts on their BSE images with a sharp boundary roughly parallel to the edge of the SMVs (Figs. 1d and 1f, Fig. 4a). The dark part consists of submicron-scale polycrystalline aggregates (herein termed ‘polycrystalline domains’), whereas the bright part is similar to H-ap in texture (herein termed ‘apatite domains’). Two domains can be more readily distinguished from their CL images, where the

polycrystalline domains have a bright, cloudy texture and the apatite domains have a relatively dark and homogeneous texture (Fig. 4b). The compositions and Raman spectra are correlated with textural variations observed between the two domains. Cl content in the apatite domains is similar to that of H-ap (~5.7 wt%) but drops down to 2.4 wt% in the polycrystalline domains. Meanwhile, $Na_2O$ content decreases from ~0.42 wt% to 0.07 wt%, and MgO content increases from less than 0.01 wt% to 0.4 wt% (Table 1, Fig. 2). The Raman spectra for the polycrystalline domains show that the peaks for apatite have been substantially weakened and replaced by tuite peaks, including an intense peak at 977 $cm^{-1}$, three less intense peaks at 412, 578, and 1096 $cm^{-1}$, and two weak peaks at 641 and 1002 $cm^{-1}$ (Fig. 3; Xie et al., 2002). The Raman spectra for the apatite domains largely retain features for apatite, although they may also contain weak tuite peaks (e.g., the 977 $cm^{-1}$ peak) at regions < 100 μm bordering the SMVs (Fig. 3). The high-resolution BSE images show that patches of residual apatite are surrounded by sub-micron tuite crystallites in the porous polycrystalline domains (Fig. 5), whereas the apatite domains largely retain a texture similar to that of H-ap.

As indicated by the BSE and CL images, the width of the polycrystalline domains of W-ap in Suizhou is generally less than 10 μm. However, even on such a small scale, the phase transformation is heterogeneous as visualized from the Raman mapping. Raman mapping of a W-ap grain displays intensity distributions of main Raman peaks at 977 $cm^{-1}$ for tuite (Fig. 4c) and at 960 $cm^{-1}$ for apatite (Fig. 4d), respectively. For the polycrystalline domain, the intensity of 977 $cm^{-1}$ peak decreases significantly from the middle part (convex into the SMVs center) to the two ends (depart from the SMVs center), and the reverse is true for the intensity distribution of the 960 $cm^{-1}$ peak. Corresponding to the Raman features, Cl content increases ~30% from the middle part to the both

ends (from 2.4 to 3.4 wt%), whereas MgO content substantially decreases (from 0.4 to 0.06 wt%).

Apatite in the SMVs (S-ap) has decomposed to polycrystalline aggregates without planar fractures as shown on BSE images (Figs 1g and 1h). Compared to the polycrystalline domains of W-ap, S-ap generally contains less residual Cl (Fig. 2; Table 1), and hence a smaller amount of relict apatite. This is also revealed by its Raman spectra that all the Raman peaks are characteristic for tuite except a residual weak peak at 960 $cm^{-1}$ for apatite (Fig. 3; Xie et al., 2002). The decomposition of S-ap is also heterogeneous, with the residual Cl content ranging from 2.9 wt% to 0.2 wt%. S-ap located close to the center of the SMVs (i.e., S-ap12) has been most thoroughly transformed to tuite.

## U–Pb dating of phosphates

Six *in situ* SIMS analyses were performed on H-ap, seven on W-ap and three on S-ap (Fig. 1; Table 2). Because mineral grains in the SMVs have largely been fragmented, only two relatively large tuite "grains" (30–40 μm) were found (Figs. 1g and 1h) after careful search of five polished sections (a total exposed area of 45 $cm^2$). Two analyses of S-ap were on a tuite inclusion in a fragment of majorite (Fig. 1g) and the other was on an individual tuite grain close to the center of the SMVs (Fig. 1h). Of the seven analyses of W-ap, six are on mixing areas with variable proportions of apatite and tuite; the other (W-ap17@3) is on an area containing exclusively apatite (Figs. 1d–f).

Apatite from large planets (e.g., Earth and Mars) could incorporate significant amounts of initial Pb (e.g., Li et al., 2012; Zhou et al., 2013), but chondritic Ca-phosphates were reported to contain negligible level of initial Pb (Göpel et al., 1994; Yin et al., 2014). This is true for Suizhou phosphates that they usually reflect very radiogenic nature with minimal evidence of an initial Pb component (most $^{206}Pb/^{204}Pb > 1000$) (Table 2). Only five analyses yield relatively high $^{206}Pb/^{204}Pb$ ratios in the

range of 170–450. Of these 5 analyses (except W-ap9@2), the $^{204}$Pb signal intensity gradually decreased until it was constant after about 7 scans (Fig. 6), suggesting a surface-related terrestrial Pb contamination probably introduced during sample preparation. For those analyses with a low level of common Pb ($^{206}$Pb/$^{204}$Pb > 1000), the $^{204}$Pb signal intensity is low and relatively constant from scan to scan (generally lower than 0.1 c/s; Fig. 6). The $^{204}$Pb signal intensity in W-ap9@2 is constant (0.3 c/s) during analysis but significantly higher than other analyses on the same grain (e.g., < 0.1 c/s for W-ap9@1; Fig. 6). This is probably due to contaminations from microcracks or non-phosphate phases. Therefore, the common Pb was corrected using the modern terrestrial Pb compositions (Stacey and Kramers, 1975), as well as CDT (Tatsumoto et al., 1973) as a limiting case for comparison (Table 2). Two different common Pb corrections result in negligible difference in calculated ages (less than 1.5‰) (Table 2). We also extracted the last 8 scans of the analyses with high common-Pb levels and recalculated their ages, but the refined ages are basically unchanged (differences less than 1‰).

Analyses of H-ap yield a concordia U–Pb age of 4547 ± 19 Ma (MSWD = 0.61, P = 0.43) on the U–Pb concordia diagram and a weighted average $^{207}$Pb/$^{206}$Pb age of 4545 ± 17 Ma (MSWD = 1.5, P = 0.2) (Figs. 7a and 7d). If only analyses with relatively low common Pb ($^{206}$Pb/$^{204}$Pb > 1000) are considered, the data yield a concordia U–Pb age of 4559 ± 26 Ma and a $^{207}$Pb/$^{206}$Pb age of 4558 ± 14 Ma. The U–Pb data of W-ap plot on a discordia line with an upper intercept age of 4525 ± 14 Ma and a lower intercept going through the original point (Fig. 7b). The apparent $^{207}$Pb/$^{206}$Pb ages of W-ap vary from 4534 to 4503 Ma if W-ap17@3 is excluded (it contains exclusively apatite; Table 2). Three analyses of S-ap yield a poorly-defined discordia line with an upper intercept age of 4513 ± 260 Ma and a lower intercept through the coordinate origin (Fig. 7c). Among the three analyses, one spot

225 (S-ap12@1), which is close to the center of the SMVs and essentially consists of tuite, yields the
226 youngest $^{207}Pb/^{206}Pb$ age of 4481 ± 30 Ma (2σ) and a comparable concordant U–Pb age of 4481 ± 30
227 Ma (2σ). The apparent $^{207}Pb/^{206}Pb$ ages of S-ap range from 4527 to 4481 Ma.

228 U–Pb analyses of partly decomposed apatite show slight normal or reverse discordance (Figs. 7b
229 and 7c) that is not correlated with the extent of apatite decomposition, thus they are probably not due
230 to matrix effects. For example, two analyses on one partly decomposed apatite (S-ap8) show both
231 notable normal and reverse discordance; while one analyse on a compeletely decomposed apatite
232 (S-ap12) yield a nearly concordant U–Pb age. We argue this could be related to several factors. First,
233 our SIMS analyses were made using a beam size of 10 × 15 μm on very small irregular shaped grains
234 (e.g., S-ap8). Although care has been taken before each measurement, the possibility of sampling
235 metal–sulfide veinlets and neighboring non-phosphate phases during SIMS analysis cannot be totally
236 excluded. This may result in calibration problems leading to uncontrolled apparent normal and reverse
237 discordance (e.g., Liu et al., 2012), and it was probably aggravated by minor contribution of
238 unsupported Pb from these non-phosphate phases (Fig. 1g). Second, the discordance may result from
239 surface imperfections of the sample due to polycrystalline nature of tuite or/and from comparing
240 samples and standards in different mounts (e.g., Liu et al., 2012). Third, the discordance may be a
241 result of residual instrumental elemental fractionation after correction to standards (e.g., Shaulis et al.,
242 2017). Forth, it is also possible that some normal discordance of partly decomposed apatite is due to
243 recent Pb loss, because the high surface area to volume ratios of these sub-micron polycrystalline
244 aggregates would facilitate surface-related Pb loss (Kamo et al., 1996). Due to these analytical
245 uncertainties and potential matrix effects, the $^{207}Pb/^{206}Pb$ ages are considered to be more reliable, as

246 they are not affected by the calibration of U/Pb ratio and are not sensitive to recent Pb loss (Misawa et
247 al., 2005).

248 # DISCUSSION

249 ## Variable response of apatite to shock metamorphism in the Suizhou chondrite

250 Apatite is a common phosphate phase present in terrestrial and extraterrestrial rocks. Because
251 apatite contains a relatively high U content and has a low closure temperature for U–Pb system, it is
252 now increasingly used for dating impact events (e.g., Grange et al., 2013; Merle et al., 2014;
253 Norman and Nemchin, 2014; Yin et al., 2014; Snape et al., 2016; Li and Hsu, 2018a; 2018b).
254 Nevertheless, there are few studies focused on the shock metamorphic features of apatite, which
255 would have an important implication for the interpretation of chronological data. Our study shows a
256 remarkable variation of chemical and structural modifications of apatite in the Suizhou chondrite that
257 corresponds to different degrees of shock metamorphism.

258 H-ap in Suizhou remains essentially intact and its Raman spectra resemble those of unshocked
259 chlorapatite (Fig. 3; Xie et al., 2013). Planar fractures observed in H-ap also exist in neighboring
260 olivine and low-Ca pyroxene grains (Figs. 1a–c), which are typical shock effects for weak to moderate
261 shock metamorphism (Stöffler et al., 1991). H-ap in Suizhou is chemically similar to apatite from
262 other weakly shocked equilibrated L chondrites, which have a Cl content of 4.43–5.68 wt%, $Na_2O$ of
263 0.33–0.49 wt% and MgO less than 0.1 wt% (Fig. 2; Lewis and Jones, 2016). The H-ap grains in
264 Suizhou appear to have largely preserved their original structural and chemical features produced
265 during the parent-body thermal metamorphism (Jones et al., 2014).

Both chemical composition and Raman spectra indicate that W-ap grains adjacent to the SMVs were partly transformed to tuite (Figs. 2 and 3). This can also be seen on their high-resolution BSE images, where patches of residual apatite are surrounded by tuite crystallites (Fig. 5). Tuite could be formed by decomposition of apatite at 1100–2300 °C and 10–15 GPa (Murayama et al., 1986). It can be stable up to 20 GPa or higher (Xie et al., 2013). This *P–T* condition is compatible with that estimated from the high-pressure mineral inventory in the SMVs of Suizhou (Xie et al., 2001; Xie and Chen, 2016). The neo-crystallized tuite is distinguished by its polycrystalline texture (Fig. 5), which can be readily identified by its cloudy appearance on the CL images (Fig. 4b). Polycrystalline (or granular) textures were also observed in zircon, baddeleyite and monazite that have been extensively shocked in natural impact events (Krogh et al., 1993; Kamo et al., 1996; Krogh et al., 1996; Moser, 1997; Zhang et al., 2011; Darling et al., 2016). In contrast to the polycrystalline textures previously observed in these U-bearing minerals, the polycrystalline aggregates reported here consist of a high-pressure phase, probably because the rapid cooling of the SMVs prohibited its back transformation to the low-pressure polymorph. The polycrystalline domains of W-ap are located exclusively adjacent to the SMVs and parallel to the edge of the SMVs (Figs. 1d and 1f). This strongly indicates their formation is induced by the localized transient heating within the SMVs, which was achieved by localized shear-friction stress (Xie and Chen, 2016). However, only restricted regions (generally less than 10 μm) of apatite can be extensively transformed (i.e., polycrystalline domains; Figs. 1d and 1f) and the phase transformation is highly heterogeneous even on such small regions (Fig. 4). It could be due to fact that the temperature gradient is very steep from the SMVs to the neighboring host in Suizhou, which is also indicated by the presence of three different polymorphs of

chromite within a single grain adjacent to the SMVs (Chen et al., 2003). As a result, at regions > 100 μm bordering the SMVs, the temperature was too low to overcome the kinetic barriers for nucleation and growth of tuite, and the apatite domains at these regions remain relatively intact.

Compared to W-ap, S-ap of Suizhou generally has a lower chlorine content and a weaker Raman peak at 960 $cm^{-1}$. S-ap would be more thoroughly transformed to polycrystalline tuite, but the phase transition of S-ap is also heterogeneous (Figs. 2 and 3). This is probably because only a small amount of shock-induced melt was generated in the relatively thin SMVs of Suizhou, and it could not generate enough heat to increase the temperature sufficiently throughout the SMVs in a short period of time (Chen et al., 2004). Therefore, at the relatively "cold" regions, such as those included in and shielded by other entrained mineral fragments in the SMVs, the decomposition of apatite is incomplete. The remnant Cl contents in these grains are up to 2.9 wt%, which are similar to those of W-ap polycrystalline domains (2.0–3.4 wt%). Whereas for portions close to the center of SMVs, the apatite could experience a higher degree of transformation (Fig. 2), which was also observed by Xie et al. (2013).

On the basis of these observations, a sequence of increasing degrees of shock metamorphism for apatite in Suizhou can be established. (1) In regions > 100 μm bordering the SMVs, including H-ap and parts of the apatite domains in W-ap, apatite was only regularly fractured and retains well-preserved chemical compositions and crystallinity. (2) In regions < 100 μm bordering the SMVs (especially within the polycrystalline domains of W-ap) or in relatively "cold" regions within the SMVs, apatite could be partly decomposed to tuite with variable amounts of apatite relics. (3) In regions close to the center of SMVs, apatite was completely transformed to polycrystalline tuite.

These different shock effects are closely related to the temperature conditions prevailing during the impact.

## Correlated impact features with the degree of isotopic disturbance in phosphates and the age of the SMVs in Suizhou

Merrillite and apatite are the major phosphates in ordinary chondrites, with a total abundance of about 0.4–0.6 vol% (Gastineau-Lyons et al., 2002). Although merrillite is much more abundant than apatite in Suizhou, U concentrations in merrillite are too low to provide meaningful U–Pb ages in our SIMS analysis. As a result, only apatite and associated tuite were investigated in this study. By integrating *in situ* chemical, microstructural and isotopic analysis of phosphates in Suizhou, it is possible to establish a correlation between the extents of isotopic disturbance with varying degrees of shock metamorphism.

H-ap grains, which have well-preserved chemical compositions and crystallinity, yield the oldest, concordia U–Pb age (4547 ± 19 Ma) that agrees well with the weighted average $^{207}Pb/^{206}Pb$ age (4545 ± 17 Ma). If only analyses with relatively low common Pb ($^{206}Pb/^{204}Pb > 1000$) are considered, they yield a slightly older U–Pb (4559 ± 26 Ma) and $^{207}Pb/^{206}Pb$ (4558 ± 14 Ma) ages. The age of H-ap in Suizhou is consistent with the U–Pb ages of phosphates previously determined with thermal ionization mass spectrometry in other unshocked L chondrites (4511 to 4543 Ma; Göpel et al., 1994). Due to the large difference in condensation temperatures for Ca and P, the apatite in ordinary chondrites were thought to have formed by fluid-assistant thermal metamorphism on their parent body (Jones et al., 2014). Therefore, the U–Pb and Pb–Pb ages of H-ap most likely record the time when apatite cooled down below its closure temperature from the peak thermal metamorphic temperature on its parent

329 body.

330 The apatite grain located in the center of SMVs (S-ap12) was most thoroughly decomposed to
331 polycrystalline tuite and its chemical compositions have been altered to the greatest extent (Fig. 2).
332 The SIMS analysis on this "grain" yields a concordia U–Pb age of 4481 ± 30 Ma (2σ) and a
333 $^{207}Pb/^{206}Pb$ age of 4481 ± 30 Ma (2σ). These ages are the youngest for all the analyzed phosphates and
334 can be readily distinguished from the U–Pb and weighted average $^{207}Pb/^{206}Pb$ ages of H-ap well
335 beyond the 2-sigma level. Other analyses of W-ap and partly decomposed S-ap, which are mixtures of
336 apatite and tuite, yield intermediate apparent $^{207}Pb/^{206}Pb$ ages from 4534 to 4503 Ma (Figs. 7b–d).

337 Our data clearly demonstrate that the disturbance of apatite U–Pb systematics in Suizhou strongly
338 correlated with the compositional and structural changes induced by shock metamorphism. The most
339 thoroughly decomposed apatite (S-ap12), which consists essentially polycrystalline tuite aggregates,
340 yields the youngest, "concordant" age of 4481 ± 30 Ma (Fig. 7c). Nevertheless, the concordia line is
341 nearly linear for this time interval (Fig. 7), making it difficult to identify possible slight discordance
342 with the precision of current SIMS analysis. This is further aggravated by the potential SIMS
343 analytical issues as mentioned earlier. As a result, the possibility of inheriting radiogenic Pb from the
344 minor residual apatite cannot be completely ruled out, and this age is best regarded as the maximum
345 age for the impact event.

346 **The prevalence of ~4.48 Ga impact events in the primordial asteroid belt**

347 Several lines of evidence indicate that major impact events occurred > 4.4 Ga on the L chondrite
348 parent body (Keil et al., 1994; Scott, 2002). For example, the cooling rates of individual metal grains
349 from the matrices of L regolith breccias exhibit a wide range (1–1000 °C/My), which indicates their

parent bodies may have been broken up and reassembled sometime between the end of slow cooling around 4.4 Ga (Taylor et al., 1987). Chronological records for very early collisional events in the solar system history are rare and sometimes ambiguous, as old impact ages could be overprinted by the contemporary or subsequent thermal metamorphism on the parent body (e.g., Weirich et al., 2010). The U–Pb systematics of phosphates in unshocked ordinary chondrites implies that the parent asteroids experienced a protracted period (~60 My) of thermal metamorphism (Göpel et al., 1994), and the phosphate U–Pb ages less than 4.5 Ga are often interpreted as impact-reset ages (Bogard, 2011; Bottke et al., 2015). The U–Pb systematics of apatite grains in Novato (L6), which define a well regressed upper intercept age of 4472 ± 31 Ma and lower intercept age of 473 ± 38 Ma, were suggested to record two impact events on the L chondrite parent body (Yin et al., 2014). A similar result was found in the phosphates of the L-impact melt breccia NWA 7251 (two impact ages at 4457 ± 56 Ma and 574 ± 82 Ma; Li and Hsu, 2018b). The phosphates in Sahara 98222 (L6), with a total Pb/U isochron age of 4467 ± 22 Ma, were also interpreted to record an early impact event (Ozawa et al., 2008). In addition, $^{39}Ar$–$^{40}Ar$ dating of the impact-melt L chondrite PAT 91501 yields a similar impact age (4461 ± 8 Ma; Benedix et al., 2008). The U–Pb ages Novato, NWA 7251 and Sahara 98222, as well as the $^{39}Ar$–$^{40}Ar$ age of PAT 91501, coupled with the estimated impact age of Suizhou, all point to a fact that early impact events (> 4.4 Ga) occurred on the parent body of L chondrite (Fig. 8). Our study provides additional robust mineralogical evidence for such impact events. In addition to L chondrites, comparable impact ages are also observed in other types of meteorite, such as H and LL groups, enstatite chondrites and HED (howardite–eucrite–diogenite) meteorites (Bogard, 2011; Popova et al., 2013; Swindle et al., 2014). These coeval impact events occurred on a variety of parent

asteroids presumably reflect a high collision rate as the accretion of planets was finishing, or speculatively result from the peak arrival time of ejecta debris from the Moon-forming giant impact at the primordial main belt (Bottke et al., 2015).

## The effects of natural shock on U–Pb isotopic systematics of apatite

Shock recovery experiments suggest that post-shock annealing plays the most important role in resetting isotopic clocks, and naturally shocked and unannealed samples are unlikely to record the timing of impact events (e.g., Fredriksson and De Carli, 1964; Bogard et al., 1987; Deutsch and Schärer, 1990; Gaffney et al., 2011; Niihara et al., 2012). However, our results clearly point to the other direction. The preservation of various metastable high-pressure phases in Suzhou indicates it could not have experienced extensive post-impact annealing after pressure release, otherwise these high-pressure phases would revert readily to their more stable low-pressure polymorphs. For example, ringwoodite in Suizhou would have totally back transformed to olivine within 1.5 hours at post shock temperature of 760 °C (Ming et al., 1991); while akimotoite would have completely decomposed at 700 °C within 1 hour at most (Ito and Navrotsky, 1985). Our observations strongly indicate a localized high-temperature pulse during shock compression is essential for disturbance of the U–Pb isotopic systematics of phosphates in Suizhou. This was also observed in the Sixiangkou L6 chondrite (Li and Hsu, 2018a).

We suggest the disparity could be mainly attributed to the different shock durations and temperature conditions between natural impact events and laboratory shock experiments. The shock-pulse duration in shock-recovery experiments is usually less than 10 μs, which is 4–6 orders of magnitudes shorter than those of natural shock events (Sharp and DeCarli, 2006; El Goresy et al.,

392 2013). Furthermore, most shock experiments were done on dense non-porous target, and the peak
393 temperature was mostly along the principal Hugoniot of those minerals, which is significantly lower
394 than the temperature experienced by the SMVs in meteorites which were naturally shocked to S4–S6
395 levels (Sharp and DeCarli, 2006). Under these extreme *P–T–t* conditions, Pb loss in apatite (and tuite)
396 appears to be more efficiently achieved. The porous texture of the decomposed apatite (Fig. 5) in
397 Suizhou implies Pb volatilization as a possible mechanism. Porous textures have been observed on the
398 shocked terrestrial zircon from K/T boundary ejecta (Bohor et al., 1993) and the fallback breccia of
399 Sudbury impact structure (Krogh et al., 1996), as well as shocked lunar zircon (Zhang et al., 2011). All
400 these shocked zircons have experienced substantial Pb loss, although zircons in the first two examples
401 have only experienced flash heating like S-ap and W-ap in Suizhou. Similar textures were also
402 reported on zircon grains experimentally heated to 1400–1650 °C under vacuum (Ansdell and Kyser,
403 1993). During the heating, Pb loss was detected with concomitant breakdown of zircon to porous
404 baddeleyite (Ansdell and Kyser, 1993). Considering the temperature in the SMVs of Suizhou could
405 have readily exceeded 2000 °C, which is much higher than the temperature required for Pb
406 evaporation in the experiment of Ansdell and Kyser (1993), we suggest volatilization could account
407 for the rapid Pb loss occurred in the phosphates of Suizhou. Alternatively, Pb loss may be achieved by
408 substantial partitioning into the newly formed chloride through the possible decomposition reaction
409 $2Ca_5(PO_4)_3Cl \rightarrow 3\gamma\text{-}Ca_3(PO_4)_2 + CaCl_2$ (Murayama et al., 1986; Xie et al., 2013). Under the *P–T*
410 conditions experienced by the SMVs of Suizhou during the impact, $CaCl_2$ would have a $PbCl_2$-type
411 structure (Léger et al., 1998). However, despite an intensive search for chloride phases, they were
412 neither detected in natural samples, nor in the products of high-pressure experiments (Murayama et al.,

1986; Xie et al., 2013). A counterpart (i.e., $CaF_2$) was also not identified in the experimental decomposition of fluorapatite by X-ray diffraction (Murayama et al., 1986). It may be possible that the fractions of these components are too small (< 10 wt%) and too widely dispersed in the polycrystalline tuite (Murayama et al., 1986); or they have been leached during the preparation of polished thin sections (Xie et al., 2013). Nevertheless, this mechanism is feasible, and it could provide an additional pathway for Pb loss from the system.

## IMPLICATIONS

Dating the high-pressure phosphates in the SMVs of Suizhou opens a new window for a comprehensive study of impact history of the Solar System. Impact dating using isotope systems is generally applied to lithologies that were almost completely molten or minerals newly crystallized from such melt, because their radioactive clocks tend to have been reset (Jourdan et al., 2009). Only relatively large parent bodies, like the Moon and Vesta, could sustain such a large impact (Bogard, 2011). Undifferentiated meteorites are most likely derived from small asteroidal bodies, on which large impacts would completely destroy their parent bodies; small impacts, on the other hand, would not be able to generate sufficient heat to reset their isotopic chronometer on a whole-rock scale (Bogard, 2011). However, small impacts could induce localized melting during shock compression. From this study, it is apparent that phosphates in the SMVs or shock melt pockets of undifferentiated meteorites could be able to record the timing of these small-scale impact events.

## ACKNOWLEDGEMENTS

We thank Xian-Hua Li, Qiu-Li Li, Yu Liu, and Guo-Qiang Tang for their assistance with the SIMS analyses. The paper benefitted from constructive reviews by Joshua Snape, Sergio Speziale, Audrey Bouvier, and an anonymous referee as well as the editorial handling of Steven Simon. This work was supported by the National Natural Science Foundation of China (Grant No. 41573059 and 4173059), the Macau FDCT (119/2017/A3, 005/2017/A1), the Minor Planet Foundation of China, and the China Postdoctoral Science Foundation (Grant No. 2017M621704).

## REFERENCES

Ansdell, K.M., and Kyser, T.K. (1993) Textural and chemical changes undergone by zircon during the Pb-evaporation technique. American Mineralogist, 78, 36–41.

Benedix, G.K., Ketcham, R.A., Wilson, L., McCoy, T.J., Bogard, D.D., Garrison, D.H., Herzog, G.F., Xue, S., Klein, J., and Middleton, R. (2008) The formation and chronology of the PAT 91501 impact-melt L chondrite with vesicle–metal–sulfide assemblages. Geochimica et Cosmochimica Acta, 72(9), 2417–2428.

Bloch, E., and Ganguly, J. (2014) $^{176}$Lu–$^{176}$Hf and $^{147}$Sm–$^{143}$Nd ages of the Martian shergottites: Evaluation of the shock-resetting hypothesis through diffusion kinetic experiments and modeling, and petrological observations. Earth and Planetary Science Letters, 395, 173–183.

Bogard, D.D. (1995) Impact ages of meteorites: A synthesis. Meteoritics, 30(3), 244–268.

——. (2011) K–Ar ages of meteorites: Clues to parent-body thermal histories. Chemie der Erde-Geochemistry, 71(3), 207–226.

Bogard, D.D., Hörz, F., and Johnson, P. (1987) Shock effects and argon loss in samples of the Leedey L6 chondrite experimentally shocked to 29–70 GPa pressures. Geochimica et Cosmochimica Acta, 51(7), 2035–2044.

Bohor, B.F., Betterton, W.J., and Krogh, T.E. (1993) Impact-shocked zircons: Discovery of shock-induced textures reflecting increasing degrees of shock metamorphism. Earth and Planetary Science Letters, 119(3), 419–424.

Bottke, W.F., Vokrouhlický, D., Marchi, S., Swindle, T., Scott, E.R.D., Weirich, J.R., and Levison, H. (2015) Dating the Moon-forming impact event with asteroidal meteorites. Science, 348(6232), 321–323.

Chen, M., Shu, J.-F., Mao, H.-k., Xie, X.-D., and Hemley, R.J. (2003) Natural occurrence and synthesis of two new postspinel polymorphs of chromite. Proceedings of the National Academy of Sciences, 100(25), 14651–14654.

462 Chen, M., Xie, X.-D., and Goresy, A.E. (2004) A shock-produced (Mg, Fe)$SiO_3$ glass in the Suizhou
463 meteorite. Meteoritics & Planetary Science, 39(11), 1797–1808.
464 Darling, J.R., Moser, D.E., Barker, I.R., Tait, K.T., Chamberlain, K.R., Schmitt, A.K., and Hyde, B.C.
465 (2016) Variable microstructural response of baddeleyite to shock metamorphism in young basaltic
466 shergottite NWA 5298 and improved U–Pb dating of Solar System events. Earth and Planetary
467 Science Letters, 444(15), 1–12.
468 Deutsch, A., and Schärer, U. (1990) Isotope systematics and shock-wave metamorphism: I. U–Pb in zircon,
469 titanite and monazite, shocked experimentally up to 59 GPa. Geochimica et Cosmochimica Acta,
470 54(12), 3427–3434.
471 Deutsch, A., and Schärer, U. (1994) Dating terrestrial impact events. Meteoritics, 29(3), 301–322.
472 El Goresy, A., Gillet, P., Miyahara, M., Ohtani, E., Ozawa, S., Beck, P., and Montagnac, G. (2013)
473 Shock-induced deformation of Shergottites: Shock-pressures and perturbations of magmatic ages
474 on Mars. Geochimica et Cosmochimica Acta, 101(15), 233–262.
475 Fredriksson, K., and De Carli, P. (1964) Shock emplaced argon in a stony meteorite: 1. Shock experiment
476 and petrology of sample. Journal of Geophysical Research, 69(7), 1403–1406.
477 Fritz, J., and Greshake, A. (2009) High-pressure phases in an ultramafic rock from Mars. Earth and
478 Planetary Science Letters, 288(3), 619–623.
479 Gaffney, A.M., Borg, L.E., Asmerom, Y., Shearer, C.K., and Burger, P.V. (2011) Disturbance of isotope
480 systematics during experimental shock and thermal metamorphism of a lunar basalt with
481 implications for Martian meteorite chronology. Meteoritics & Planetary Science, 46(1), 35–52.
482 Gastineau-Lyons, H.K., McSween, H.Y., and Gaffey, M.J. (2002) A critical evaluation of oxidation versus
483 reduction during metamorphism of L and LL group chondrites, and implications for asteroid
484 spectroscopy. Meteoritics & Planetary Science, 37(1), 75–89.
485 Gillet, P., and El Goresy, A. (2013) Shock events in the solar system: The message from minerals in
486 terrestrial planets and asteroids. Annual Review of Earth and Planetary Sciences, 41, 257–285.
487 Goldmann, A., Brennecka, G., Noordmann, J., Weyer, S., and Wadhwa, M. (2015) The uranium isotopic
488 composition of the Earth and the Solar System. Geochimica et Cosmochimica Acta, 148, 145–158.
489 Göpel, C., Manhes, G., and Allegre, C.J. (1994) U–Pb systematics of phosphates from equilibrated ordinary
490 chondrites. Earth and Planetary Science Letters, 121(1–2), 153–171.
491 Grange, M.L., Nemchin, A.A., and Pidgeon, R.T. (2013) The effect of 1.9 and 1.4 Ga impact events on 4.3
492 Ga zircon and phosphate from an Apollo 15 melt breccia. Journal of Geophysical Research:
493 Planets, 118(10), 2180–2197.
494 Ito, E., and Navrotsky, A. (1985) $MgSiO_3$ ilmenite: Calorimetry, phase equilibria, and decomposition at
495 atmospheric pressure. American Mineralogist, 70(9–10), 1020–1026.
496 Jones, R.H., McCubbin, F.M., Dreeland, L., Guan, Y., Burger, P.V., and Shearer, C.K. (2014) Phosphate
497 minerals in LL chondrites: A record of the action of fluids during metamorphism on ordinary
498 chondrite parent bodies. Geochimica et Cosmochimica Acta, 132(1), 120–140.
499 Jourdan, F., Renne, P.R., and Reimold, W.U. (2009) An appraisal of the ages of terrestrial impact structures.
500 Earth and Planetary Science Letters, 286(1), 1–13.
501 Kamo, S.L., Reimold, W.U., Krogh, T.E., and Colliston, W.P. (1996) A 2.023 Ga age for the Vredefort
502 impact event and a first report of shock metamorphosed zircons in pseudotachylitic breccias and

503 granophyre. Earth and Planetary Science Letters, 144(3), 369–387.
504 Keil, K., Haack, H., and Scott, E. (1994) Catastrophic fragmentation of asteroids: Evidence from meteorites.
505 Planetary and Space Science, 42(12), 1109–1122.
506 Krogh, T.E., Kamo, S.L., and Bohor, B.F. (1993) Fingerprinting the K/T impact site and determining the
507 time of impact by U–Pb dating of single shocked zircons from distal ejecta. Earth and Planetary
508 Science Letters, 119(3), 425–429.
509 ——. (1996) Shock Metamorphosed Zircons With Correlated U–Pb Discordance and Melt Rocks With
510 Concordant Protolith Ages Indicate an Impact Origin for the Sudbury Structure. In A. Basu, and S.
511 Hart, Eds. Earth Processes: Reading the Isotopic Code, p. 343–353. American Geophysical Union.
512 Langenhorst, F., and Poirier, J.-P. (2000) Anatomy of black veins in Zagami: Clues to the formation of
513 high-pressure phases. Earth and Planetary Science Letters, 184(1), 37–55.
514 Léger, J.-M., Haines, J., and Danneels, C. (1998) Phase transition sequence induced by high-pressure in
515 $CaCl_2$. Journal of Physics and Chemistry of Solids, 59(8), 1199–1204.
516 Lewis, J.A., and Jones, R.H. (2016) Phosphate and feldspar mineralogy of equilibrated L chondrites: The
517 record of metasomatism during metamorphism in ordinary chondrite parent bodies. Meteoritics &
518 Planetary Science, 51(10), 1886–1913.
519 Li, Q.-L., Li, X.-H., Wu, F.-Y., Yin, Q.-Z., Ye, H.-M., Liu, Y., Tang, G.-Q., and Zhang, C.-L. (2012) In-situ
520 SIMS U–Pb dating of phanerozoic apatite with low U and high common Pb. Gondwana Research,
521 21(4), 745–756.
522 Li, S.-L., and Hsu, W.-B. (2018a) The nature of the L chondrite parent body's disruption as deduced from
523 high-pressure phases in the Sixiangkou L6 chondrite. Meteoritics & Planetary Science, DOI:
524 10.1111/maps.13110.
525 Li, Y., and Hsu, W.-B. (2018b) Multiple impact events on the L-chondritic parent body: Insights from SIMS
526 U–Pb dating of Ca-phosphates in the NWA 7251 L-melt breccia. Meteoritics & Planetary Science,
527 DOI: 10.1111/maps.13061.
528 Litasov, K.D., and Podgornykh, N.M. (2017) Raman spectroscopy of various phosphate minerals and
529 occurrence of tuite in the Elga IIE iron meteorite. Journal of Raman Spectroscopy, 48(11), 1518–
530 1527.
531 Liu, D.-Y., Jolliff, B.L., Zeigler, R.A., Korotev, R.L., Wan, Y.-S., Xie, H.-Q., Zhang, Y.-H., Dong, C.-Y.,
532 and Wang, W. (2012) Comparative zircon U–Pb geochronology of impact melt breccias from
533 Apollo 12 and lunar meteorite SaU 169, and implications for the age of the Imbrium impact. Earth
534 and Planetary Science Letters, 319, 277–286.
535 Liu, Y., Li, Q.-L., Tang, G.-Q., Li, X.-H., and Yin, Q.-Z. (2015) Towards higher precision SIMS U–Pb
536 zircon geochronology via dynamic multi-collector analysis. Journal of Analytical Atomic
537 Spectrometry, 30(4), 979–985.
538 Liu, Y., Li, X.-H., Li, Q.-L., Tang, G.-Q., and Yin, Q.-Z. (2011) Precise U–Pb zircon dating at a scale of < 5
539 micron by the CAMECA 1280 SIMS using a Gaussian illumination probe. Journal of Analytical
540 Atomic Spectrometry, 26(4), 845–851.
541 Ludwig, K.R. (2012) Isoplot 3.75, a geochronological toolkit for Microsoft Excel. Special Publication No.
542 5. Berkeley Geochronology Center, California.
543 Merle, R.E., Nemchin, A.A., Grange, M.L., Whitehouse, M.J., and Pidgeon, R.T. (2014) High resolution

U–Pb ages of Ca-phosphates in Apollo 14 breccias: Implications for the age of the Imbrium impact. Meteoritics & Planetary Science, 49(12), 2241–2251.

Ming, L.-C., Kim, Y.-H., Manghnani, M.H., Usha-Devi, S., Ito, E., and Xie, H.-S. (1991) Back transformation and oxidation of $(Mg, Fe)_2SiO_4$ spinels at high temperatures. Physics and Chemistry of Minerals, 18(3), 171–179.

Misawa, K., Yamaguchi, A., and Kaiden, H. (2005) U–Pb and $^{207}Pb$–$^{206}Pb$ ages of zircons from basaltic eucrites: Implications for early basaltic volcanism on the eucrite parent body. Geochimica et cosmochimica acta, 69(24), 5847–5861.

Moser, D.E. (1997) Dating the shock wave and thermal imprint of the giant Vredefort impact, South Africa. Geology, 25(1), 7–10.

Murayama, J.K., Nakai, S., Kato, M., and Kumazawa, M. (1986) A dense polymorph of $Ca_3(PO_4)_2$: A high pressure phase of apatite decomposition and its geochemical significance. Physics of the Earth and Planetary Interiors, 44(4), 293–303.

Niihara, T., Kaiden, H., Misawa, K., Sekine, T., and Mikouchi, T. (2012) U–Pb isotopic systematics of shock-loaded and annealed baddeleyite: Implications for crystallization ages of Martian meteorite shergottites. Earth and Planetary Science Letters, 341–344, 195–210.

Norman, M.D., and Nemchin, A.A. (2014) A 4.2 billion year old impact basin on the Moon: U–Pb dating of zirconolite and apatite in lunar melt rock 67955. Earth and Planetary Science Letters, 388(15), 387–398.

Ozawa, S., Ohtani, E., Suzuki, A., Miyahara, M., Terada, K., and Kimura, M. (2008) Pressure-temperature conditions and U–Pb ages of shock melt veins in L6 chondrites (abstract #5042). 71st Annual Meeting of the Meteoritical Society, Matsue.

Popova, O.P., Jenniskens, P., Emel'yanenko, V., Kartashova, A., Biryukov, E., Khaibrakhmanov, S., Shuvalov, V., Rybnov, Y., Dudorov, A., Grokhovsky, V.I., Badyukov, D.D., Yin, Q.-Z., Gural, P.S., Albers, J., Granvik, M., Evers, L.G., Kuiper, J., Kharlamov, V., Solovyov, A., Rusakov, Y.S., Korotkiy, S., Serdyuk, I., Korochantsev, A.V., Larionov, M.Y., Glazachev, D., Mayer, A.E., Gisler, G., Gladkovsky, S.V., Wimpenny, J., Sanborn, M.E., Yamakawa, A., Verosub, K.L., Rowland, D.J., Roeske, S., Botto, N.W., Friedrich, J.M., Zolensky, M.E., Le, L., Ross, D., Ziegler, K., Nakamura, T., Ahn, I., Lee, J.I., Zhou, Q., Li, X.-H., Li, Q.-L., Liu, Y., Tang, G.-Q., Hiroi, T., Sears, D., Weinstein, I.A., Vokhmintsev, A.S., Ishchenko, A.V., Schmitt-Kopplin, P., Hertkorn, N., Nagao, K., Haba, M.K., Komatsu, M., and Mikouchi, T. (2013) Chelyabinsk Airburst, Damage Assessment, Meteorite Recovery, and Characterization. Science, 342(6162), 1069–1073.

Scott, E.R.D. (2002) Meteorite evidence for the accretion and collisional evolution of asteroids. In W.F. Bottke, A. Cellino, P. Paolicchi, and R.P. Binzel, Eds. Asteroids III, p. 697–709. University of Arizona Press, Tucson.

Sharp, T.G., and DeCarli, P.S. (2006) Shock effects in meteorites. In D.S. Lauretta, H.Y. McSween, and R.P. Binzel, Eds. Meteorites and the Early Solar System II, p. 653–677. University of Arizona Press, Tucson.

Shaulis, B.J., Righter, M., Lapen, T.J., Jolliff, B.L., and Irving, A.J. (2017) 3.1 Ga crystallization age for magnesian and ferroan gabbro lithologies in the Northwest Africa 773 clan of lunar meteorites. Geochimica et Cosmochimica Acta, 213, 435–456.

Snape, J.F., Nemchin, A.A., Grange, M.L., Bellucci, J.J., Thiessen, F., and Whitehouse, M.J. (2016) Phosphate ages in Apollo 14 breccias: Resolving multiple impact events with high precision U–Pb SIMS analyses. Geochimica et Cosmochimica Acta, 174, 13–29.

Stacey, J.S., and Kramers, J.D. (1975) Approximation of terrestrial lead isotope evolution by a two-stage model. Earth and Planetary Science Letters, 26(2), 207–221.

Stöffler, D., Keil, K., and Scott, E.R.D. (1991) Shock metamorphism of ordinary chondrites. Geochimica et Cosmochimica Acta, 55(12), 3845–3867.

Swindle, T.D., Kring, D.A., and Weirich, J.R. (2014) $^{40}Ar/^{39}Ar$ ages of impacts involving ordinary chondrite meteorites. Geological Society, London, Special Publications, 378(1), 333–347.

Tatsumoto, M., Knight, R.J., and Allegre, C.J. (1973) Time differences in the formation of meteorites as determined from the ratio of lead-207 to lead-206. Science, 180(4092), 1279–1283.

Taylor, G.J., Maggiore, P., Scott, E.R., Rubin, A.E., and Keil, K. (1987) Original structures, and fragmentation and reassembly histories of asteroids: Evidence from meteorites. Icarus, 69(1), 1–13.

Trotter, J.A., and Eggins, S.M. (2006) Chemical systematics of conodont apatite determined by laser ablation ICPMS. Chemical Geology, 233(3), 196–216.

Weirich, J.R., Wittmann, A., Isachsen, C.E., Rumble, D., Swindle, T.D., and Kring, D.A. (2010) The Ar–Ar age and petrology of Miller Range 05029: Evidence for a large impact in the very early solar system. Meteoritics & Planetary Science, 45(12), 1868–1888.

Xie, X.-D., and Chen, M. (2016) Suizhou Meteorite: Mineralogy and Shock Metamorphism. 258 p. Springer Berlin Heidelberg Press, Heidelberg, Germany.

Xie, X.-D., Chen, M., and Wang, D.-Q. (2001) Shock-related mineralogical features and P–T history of the Suizhou L6 chondrite. European Journal of Mineralogy, 13(6), 1177–1190.

Xie, X.-D., Minitti, M.E., Chen, M., Mao, H.-k., Wang, D.-Q., Shu, J.-F., and Fei, Y.-W. (2002) Natural high-pressure polymorph of merrillite in the shock veins of the Suizhou meteorite. Geochimica et Cosmochimica Acta, 66(13), 2439–2444.

Xie, X.-D., Zhai, S.-M., Chen, M., and Yang, H.-X. (2013) Tuite, $\gamma$-$Ca_3(PO_4)_2$, formed by chlorapatite decomposition in a shock vein of the Suizhou L6 chondrite. Meteoritics & Planetary Science, 48 (8), 1515–1523.

Yin, Q.-Z., Zhou, Q., Li, Q.-L., Li, X.-H., Liu, Y., Tang, G.-Q., Krot, A.N., and Jenniskens, P. (2014) Records of the Moon-forming impact and the 470 Ma disruption of the L chondrite parent body in the asteroid belt from U–Pb apatite ages of Novato (L6). Meteoritics & Planetary Science, 49(8), 1426–1439.

Zhang, A.-C., Hsu, W.-B., Li, X.-H., Ming, H.-L., Li, Q.-L., Liu, Y., and Tang, G.-Q. (2011) Impact melting of lunar meteorite Dhofar 458: Evidence from polycrystalline texture and decomposition of zircon. Meteoritics & Planetary Science, 46(1), 103–115.

Zhou, Q., Herd, C.D., Yin, Q.-Z., Li, X.-H., Wu, F.-Y., Li, Q.-L., Liu, Y., Tang, G.-Q., and McCoy, T.J. (2013) Geochronology of the Martian meteorite Zagami revealed by U–Pb ion probe dating of accessory minerals. Earth and Planetary Science Letters, 374, 156–163.

Zhou, Q., Yin, Q.Z., Shearer, C.K., Li, X.H., Li, Q.L., Liu, Y., Tang, G.Q., and Li, C.L. (2018) U–Pb and Pb–Pb apatite ages for Antarctic achondrite Graves Nunataks 06129. Meteoritics & Planetary

626 Science, 53(3), 448–466.

# Figure captions

Fig. 1 BSE images of apatite and associated tuite in Suizhou. (**a**)–(**c**) Apatite in the host. (**d**)–(**f**) Apatite and tuite in the vicinity of the SMVs, and the polycrystalline domains of W-ap in (**d**) and (**f**) delineated by dashed lines. (**g**) Tuite included in a majorite fragment of the SMVs and (**h**) an individual tuite "grain" in the SMVs. The ellipses with digits in panels (**a**)–(**h**) mark the SIMS analysis locations, corresponding to the data in Table 2. Ap = apatite, Ol = olivine, Pyx = low-Ca pyroxene, Pl = plagioclase, Mer = merrillite, Fe–Ni = Fe–Ni metal, Msk = maskelynite, Rwd = ringwoodite, Maj = majorite, Lgt = lingunite, Grt = garnet, Mws = magnesiowüstite, Tu = tuite.

Fig. 2 Compositions of phosphates in Suizhou. Different colors used here as well as those in Figs. 3, 4 and 7 represent "grains" of H-ap (blue), W-ap (green), and S-ap (red), respectively. Decreasing scales of grey fields represent Cl, $Na_2O$, and MgO contents of apatite from other unbrecciated L chondrites from Lewis and Jones (2016), respectively.

Fig. 3 Representative Raman spectra of phosphates from different locations of Suizhou. The sampling sites of W-ap are marked by the red spots in Fig. 4a. Vertical dashed lines represent Raman peaks for tuite.

Fig. 4 The structure of one apatite grain (W-ap9) adjacent to the SMVs in Suizhou, as revealed by BSE image (**a**), CL image (**b**) and the intensity distributions of main Raman peak of tuite at 977 $cm^{-1}$ (**c**) and apatite at 960 $cm^{-1}$ (**d**).

Fig. 5 High-magnification image of the polycrystalline domains in a W-ap grain.

Fig. 6 $^{204}$Pb intensity variation during SIMS analysis.

Fig. 7 U–Pb analyses of phosphates in different locations of Suizhou, including H-ap (**a**), W-ap (**b**) and S-ap (**c**); (**d**) $^{207}$Pb/$^{206}$Pb ages of phosphates in different locations, which are marked by different colors; analyses with high common Pb ($^{206}$Pb/$^{204}$Pb < 1000) are indicated by slashes. The gray bands in panel (**d**) show the error at the 95% confidence level of the weighted average $^{207}$Pb/$^{206}$Pb ages.

Fig. 8 Comparison of the nearly coeval impact ages of Suizhou and other meteorites. Data for other meteorites are from Bogard (2011), Popova et al. (2013), Swindle et al. (2014) and references therein.

This is a preprint, the final version is subject to change, of the American Mineralogist (MSA)
Cite as Authors (Year) Title. American Mineralogist, in press.
DOI: https://doi.org/10.2138/am-2018-6582

659 Table 1. Representative electron microprobe analyses of phosphates in Suizhou (data in wt%).

| | H-ap | | W-ap | | | | S-ap | |
|---|---|---|---|---|---|---|---|---|
| | | | apatite domains | | polycrystalline domains | | | |
| CaO | 53.3(1) | 52.8(1) | 53.5(1) | 53.4(1) | 52.9(1) | 52.8(1) | 53.0(1) | 52.7(1) |
| $Na_2O$ | 0.43(2) | 0.40(2) | 0.50(2) | 0.40(2) | 0.11(1) | 0.07(1) | 0.08(1) | 0.12(1) |
| FeO | 0.06(1) | 0.15(1) | 0.28(2) | 0.21(2) | 1.08(5) | 1.27(5) | 1.17(5) | 1.36(6) |
| MnO | 0.03(1) | b.d. | b.d. | b.d. | b.d. | b.d. | b.d. | b.d. |
| MgO | b.d. | b.d. | b.d. | b.d. | 0.04(1) | 0.05(1) | 0.12(1) | 0.85(8) |
| $Ce_2O_3$ | b.d. | b.d. | b.d. | b.d. | b.d. | b.d. | b.d. | b.d. |
| $P_2O_5$ | 41.0(1) | 40.7(1) | 41.6(1) | 41.3(1) | 41.7(1) | 41.3(1) | 42.3(1) | 42.8(1) |
| Cl | 5.93(3) | 5.59(3) | 5.64(3) | 5.63(3) | 3.13(2) | 3.41(2) | 2.19(2) | 0.23(2) |
| F | 0.43(4) | 0.37(4) | 0.39(4) | 0.34(3) | 0.42(4) | 0.22(3) | 0.16(2) | b.d. |
| -O=F,Cl | 1.52 | 1.42 | 1.43 | 1.41 | 0.88 | 0.86 | 0.56 | 0.05 |
| Total | 99.67 | 98.64 | 100.44 | 99.82 | 98.45 | 98.2 | 98.47 | 98.02 |

660 Notes: H-, W- and S-ap represent apatite (or precursor) located in the chondrite host, on the wall of SMVs,
661 and in the SMVs, respectively. b.d. = below detection limit. Numbers inside of parentheses correspond to
662 absolute uncertainties (1σ) for the last digit.

This is a preprint, the final version is subject to change, of the American Mineralogist (MSA)
Cite as Authors (Year) Title. American Mineralogist, in press.
DOI: https://doi.org/10.2138/am-2018-6582

Table 2. SIMS U–Pb isotopic data of phosphates in Suizhou.

| Analytical spot | U (ppm) | Th (ppm) | Th/U | $^{204}$Pb (c/s) | $^{206}$Pb/$^{204}$Pb | ±1σ (%) | $^{207}$Pb/$^{206}$Pb | ±1σ (%) | $^{207}$Pb*/$^{235}$U | ±1σ (%) | $^{206}$Pb*/$^{238}$U | ±1σ (%) | $^{207}$Pb*/$^{206}$Pb* | ±1σ (%) | Discordance (%) | $^{207}$Pb*/$^{206}$Pb* date (Ma) | ±1σ (Ma) | $^{207}$Pb*/$^{206}$Pb* date (Ma) # | ±1σ (Ma) |
|---|---|---|---|---|---|---|---|---|---|---|---|---|---|---|---|---|---|---|---|
| H-ap1@1 | 7.2 | 7.2 | 1.00 | 0.022 | 1235 | 26 | 0.6284 | 1.0 | 82.7 | 4.3 | 0.960 | 4.2 | 0.6252 | 1.1 | -6.9 | 4567 | 15 | 4566 | 15 |
| H-ap1@2 | 6.0 | 6.6 | 1.11 | 0.039 | 1166 | 23 | 0.6237 | 0.8 | 90.3 | 3.8 | 1.056 | 3.7 | 0.6203 | 0.8 | 2.8 | 4555 | 12 | 4554 | 12 |
| H-ap1@3 | 5.5 | 6.1 | 1.12 | 0.121 | 355 | 18 | 0.6217 | 0.9 | 88.6 | 3.8 | 1.054 | 3.7 | 0.6098 | 1.0 | 3.3 | 4531 | 14 | 4528 | 14 |
| H-ap2@1 | 5.7 | 6.3 | 1.10 | 0.094 | 361 | 16 | 0.6208 | 0.9 | 83.6 | 3.9 | 0.996 | 3.8 | 0.6091 | 1.0 | -2.3 | 4529 | 15 | 4526 | 15 |
| H-ap2@2 | 5.8 | 5.8 | 1.00 | 0.076 | 446 | 17 | 0.6173 | 0.9 | 92.1 | 3.9 | 1.099 | 3.8 | 0.6078 | 1.0 | 8.0 | 4526 | 15 | 4524 | 15 |
| H-ap3@1 | 6.4 | 7.0 | 1.09 | 0.031 | 1658 | 22 | 0.6228 | 0.8 | 98.2 | 5.6 | 1.149 | 5.6 | 0.6200 | 0.8 | 11.8 | 4555 | 12 | 4554 | 12 |
| W-ap9@1 | 7.0 | 7.1 | 1.02 | n.d. | > 10000 | − | 0.5983 | 0.8 | 86.9 | 3.9 | 1.054 | 3.8 | 0.5982 | 0.8 | 4.2 | 4503 | 12 | 4503 | 12 |
| W-ap9@2 | 6.8 | 6.6 | 0.98 | 0.319 | 173 | 6 | 0.6336 | 0.8 | 88.0 | 3.8 | 1.048 | 3.7 | 0.6091 | 1.0 | 2.8 | 4529 | 15 | 4523 | 14 |
| W-ap9@3 | 7.0 | 6.5 | 0.92 | n.d. | > 10000 | − | 0.6052 | 1.2 | 86.5 | 3.9 | 1.037 | 3.7 | 0.6051 | 1.2 | 2.0 | 4519 | 17 | 4519 | 17 |
| W-ap17@1 | 6.6 | 6.3 | 0.95 | 0.014 | 3236 | 25 | 0.6126 | 0.9 | 95.2 | 3.9 | 1.130 | 3.7 | 0.6113 | 0.9 | 10.7 | 4534 | 14 | 4534 | 14 |
| W-ap17@3 | 5.4 | 5.8 | 1.08 | 0.132 | 310 | 13 | 0.6359 | 0.9 | 94.1 | 3.8 | 1.095 | 3.6 | 0.6231 | 1.1 | 6.4 | 4562 | 15 | 4558 | 15 |
| W-ap22@1 | 9.3 | 9.3 | 1.00 | n.d. | > 10000 | − | 0.6042 | 1.0 | 71.8 | 4.4 | 0.862 | 4.3 | 0.6042 | 1.0 | -15.1 | 4517 | 14 | 4517 | 14 |
| W-ap22@2 | 6.1 | 5.7 | 0.94 | 0.006 | 4421 | 19 | 0.6095 | 1.1 | 90.3 | 4.1 | 1.076 | 3.9 | 0.6085 | 1.1 | 5.6 | 4527 | 16 | 4527 | 16 |
| S-ap8@1 | 6.6 | 6.5 | 0.98 | 0.044 | 1007 | 15 | 0.6117 | 1.2 | 100.4 | 6.2 | 1.199 | 6.1 | 0.6074 | 1.2 | 17.8 | 4525 | 17 | 4524 | 17 |
| S-ap8@2 | 6.0 | 7.2 | 1.19 | 0.014 | 1825 | 14 | 0.6108 | 1.1 | 66.0 | 4.6 | 0.787 | 4.5 | 0.6085 | 1.1 | -22.8 | 4527 | 16 | 4527 | 16 |
| S-ap12@1 | 5.8 | 6.4 | 1.10 | 0.004 | 6543 | 18 | 0.5901 | 1.0 | 80.1 | 3.9 | 0.986 | 3.7 | 0.5894 | 1.0 | -1.9 | 4481 | 15 | 4481 | 15 |

Notes: * denotes radiogenic, i.e., common Pb corrected. The common Pb was corrected using the modern terrestrial Pb compositions (Stacey and Kramers, 1975) except the apparent $^{207}$Pb/$^{206}$Pb ages in the last two columns (superscript by #), which were corrected using Pb compositions of Cañon Diablo Troilite (Tatsumoto et al., 1973). U concentrations are determined by corresponding variations of $UO_2^+/^{40}Ca_2{}^{31}P^{16}O_3^+$ ratios of Durango apatite with average 9 ppm U. $^{206}$Pb/$^{204}$Pb > 10000 means no $^{204}$Pb was detected.

This is a preprint, the final version is subject to change, of the American Mineralogist (MSA)
Cite as Authors (Year) Title. American Mineralogist, in press.
DOI: https://doi.org/10.2138/am-2018-6582

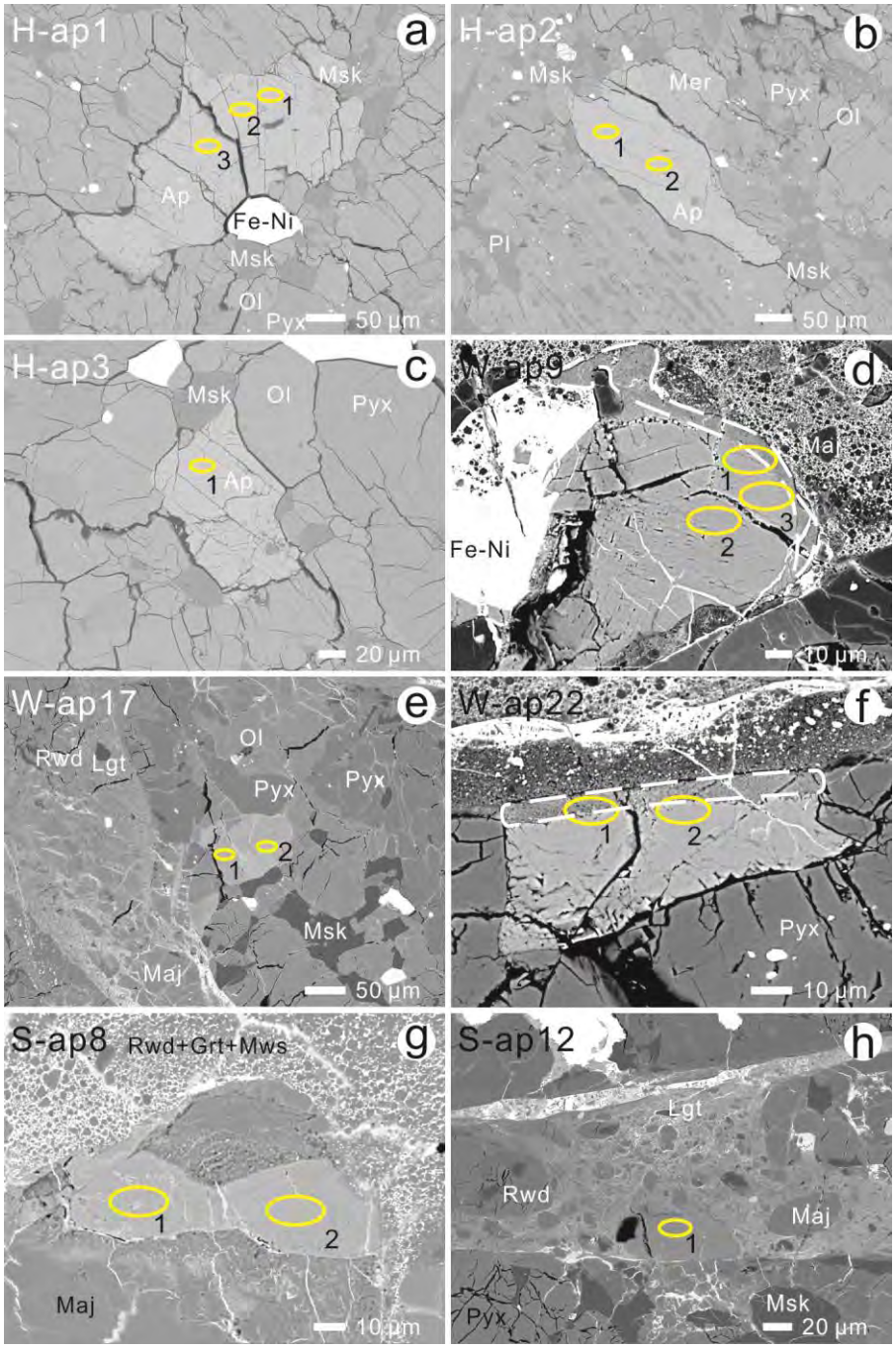


667

668 Fig. 1

669

This is a preprint, the final version is subject to change, of the American Mineralogist (MSA)
Cite as Authors (Year) Title. American Mineralogist, in press.
DOI: https://doi.org/10.2138/am-2018-6582

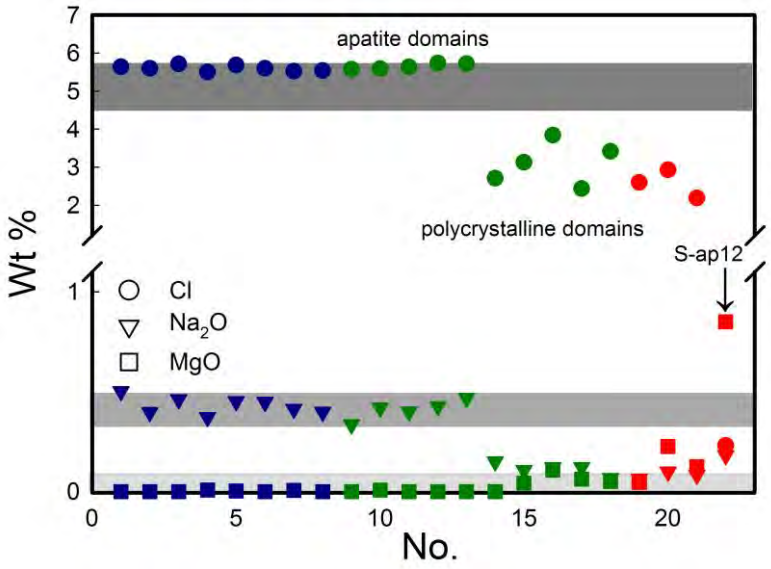


670

671 Fig. 2

672

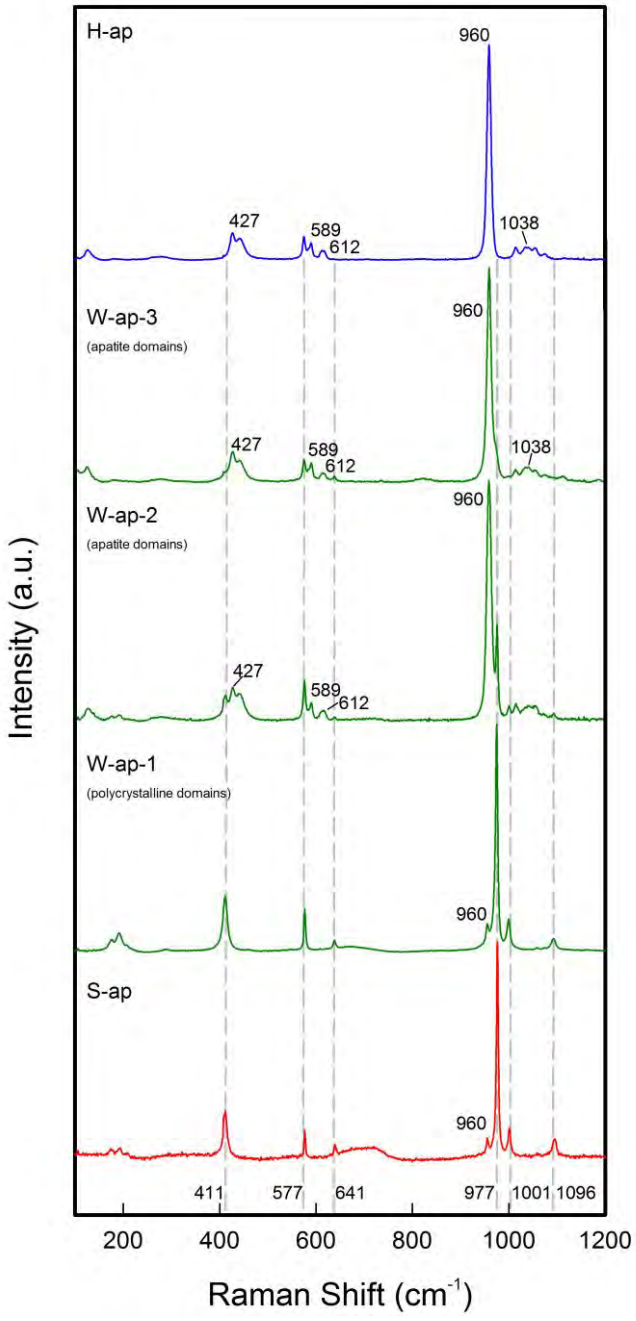


673

674 Fig. 3

675

This is a preprint, the final version is subject to change, of the American Mineralogist (MSA)
Cite as Authors (Year) Title. American Mineralogist, in press.
DOI: https://doi.org/10.2138/am-2018-6582

676

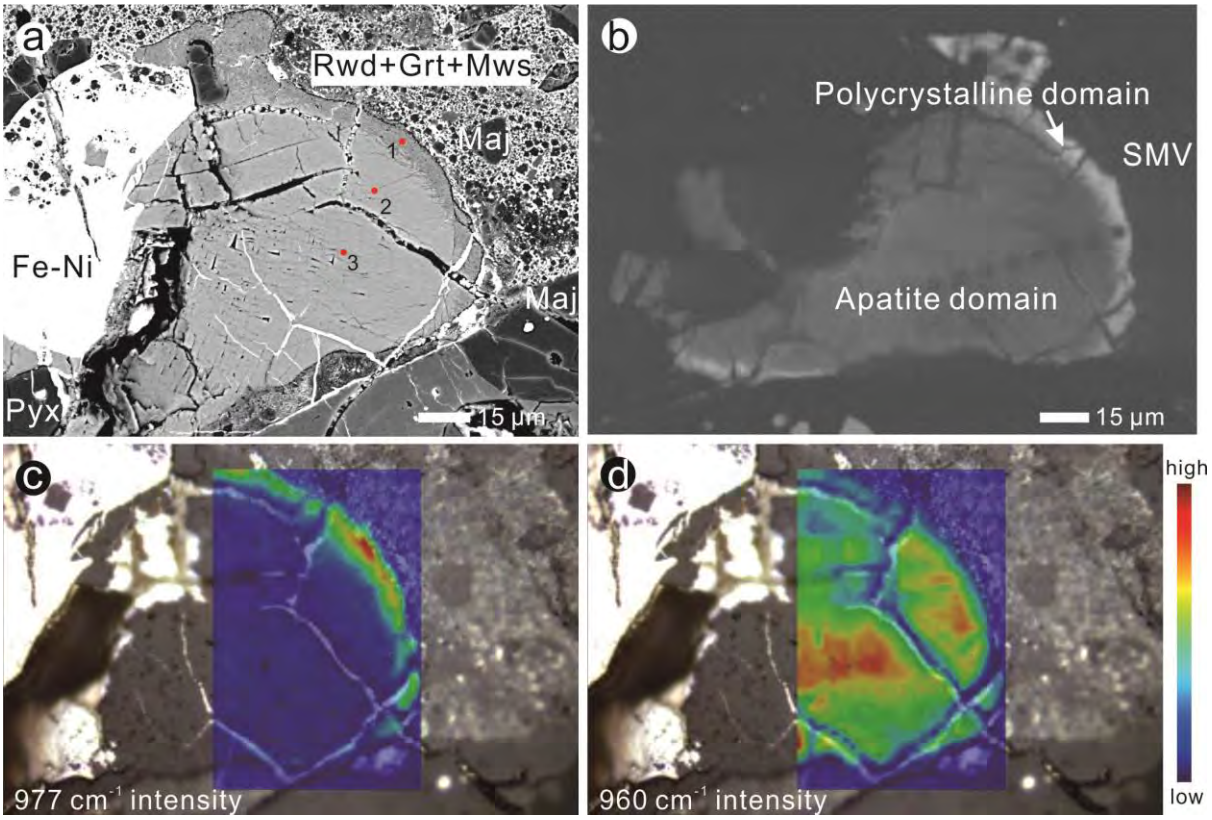


677

678 Fig. 4

679

This is a preprint, the final version is subject to change, of the American Mineralogist (MSA)
Cite as Authors (Year) Title. American Mineralogist, in press.
DOI: https://doi.org/10.2138/am-2018-6582

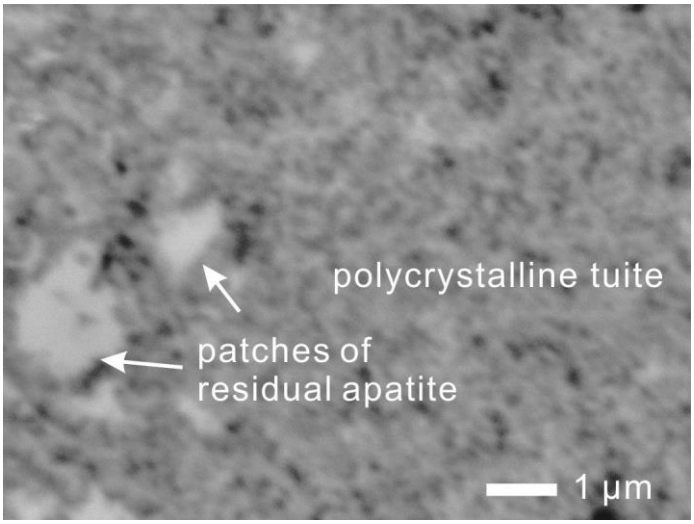


680

681 Fig. 5

682

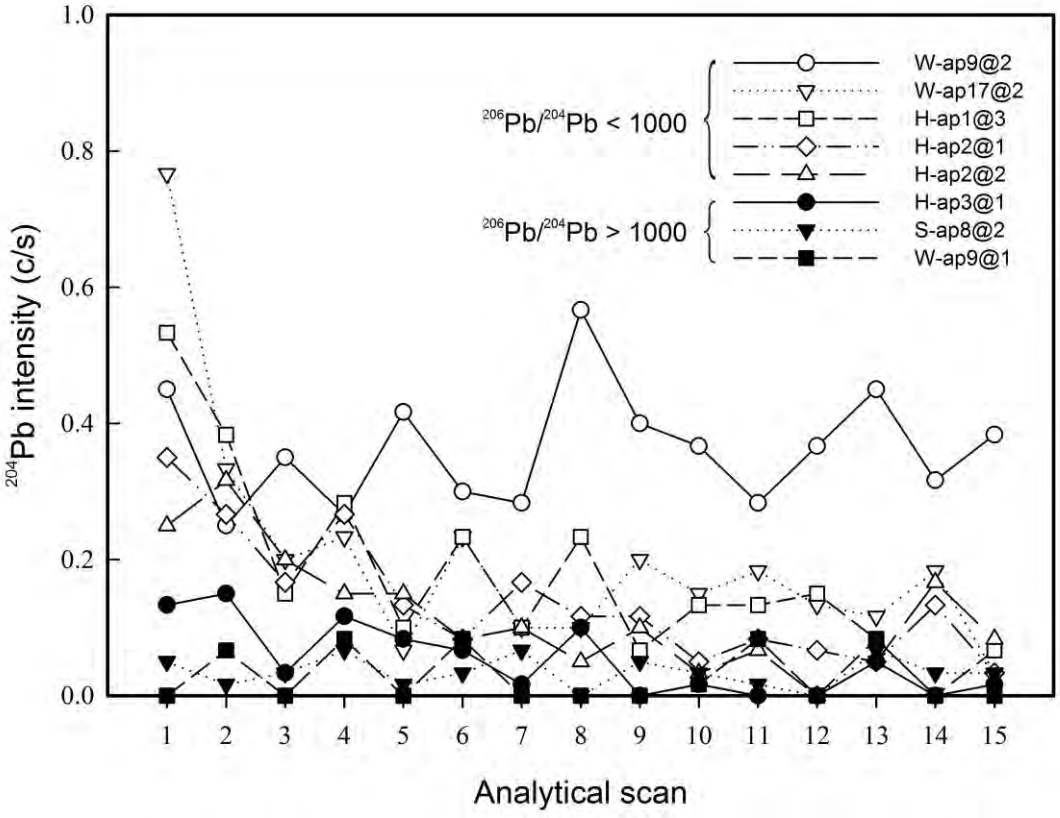


683

684 Fig. 6

685

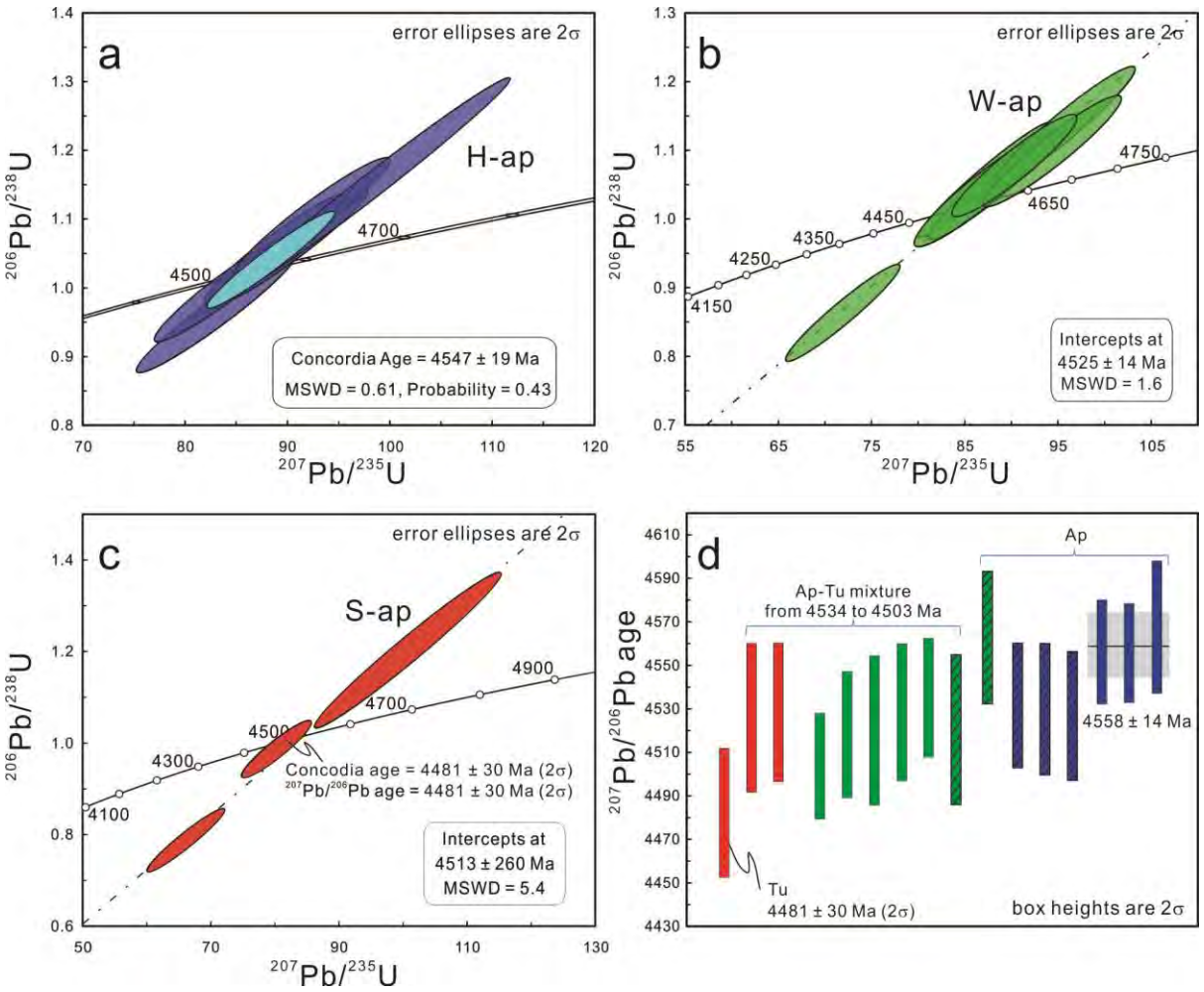


686

687 Fig. 7

688

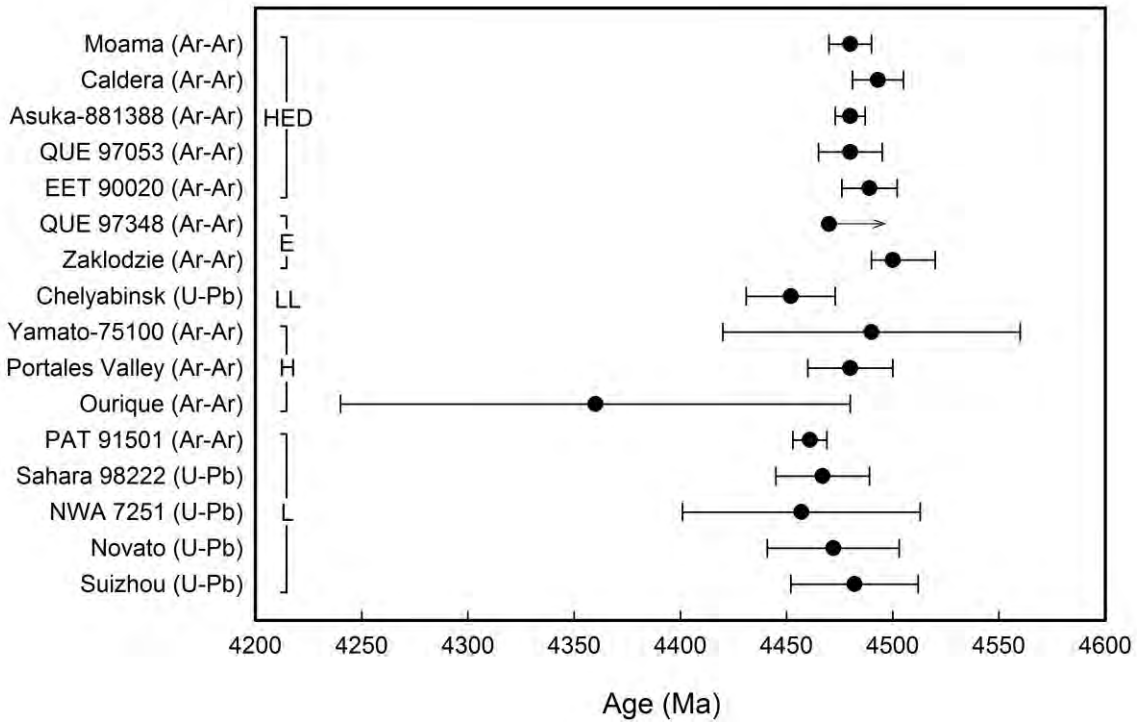


689

690 Fig. 8